RSC Advances

PAPER

View Article Online
View Journal | View Issue

CrossMark click for updates

Cite this: *RSC Adv.*, 2016, **6**, 48109

Quantum dot sensitized electrospun mesoporous titanium dioxide hollow nanofibers for photocatalytic applications†

Narendra Singh,[a] Kunal Mondal,[a] Mrinmoy Misra,[a] Ashutosh Sharma[ab] and Raju Kumar Gupta*[ab]

In this work, mesoporous, hollow TiO_2 nanofibers were fabricated by a coaxial electrospinning technique for the photocatalytic degradation of *para*-nitrophenol (4-NP), a well-known model water pollutant dye. The as-synthesized hollow nanofibers were sensitized by cadmium sulphide (CdS) quantum dots (QDs) through successive ion layer adsorption and reaction (SILAR) method for different deposition cycles. The CdS QDs loaded hollow TiO_2 nanofibers (TiO_2/CdS) harvest catalytic spots at the QDs and TiO_2 interface which helps in enhanced exciton separation. The hollow and porous TiO_2/CdS photocatalyst enhances absorption of UV and visible light due to presence of CdS QDs on the nanofiber surfaces. The resultant CdS QDs synthesized hollow TiO_2 nanofibers exhibit excellent photocatalytic activity as shown with the degradation of 4-NP dye in aqueous medium. The photocatalytic degradation study was probed spectrophotometrically by measuring the absorbance of the degraded 4-NP solution using a UV-Vis absorption spectrophotometer. The effect of CdS QDs deposition cycles on dye degradation performance was also studied for TiO_2/CdS nanofibers. TiO_2/CdS photocatalyst for 3 SILAR deposition cycles was found to be ~3 times more efficient than hollow TiO_2 nanofibers and ~8 times effective than the solid nanofibers. These nanofibers are reusable and their nanostructures do not change after repetitive usage. Such pristine and QDs sensitized hollow TiO_2 nanofibers are thus a promising platform for the development of photocatalytic wastewater treatment and other applications such as photocatalytic water splitting, sensors, Li-ion batteries, and supercapacitor electrodes.

Received 17th February 2016
Accepted 24th April 2016

DOI: 10.1039/c6ra04305d

www.rsc.org/advances

Open Access Article. Published on 26 April 2016. Downloaded on 7/28/2025 12:12:42 PM.
This article is licensed under a Creative Commons Attribution-NonCommercial 3.0 Unported Licence.

1. Introduction

Industrialisation has resulted in different types of pollutions such as water and air pollution, which are a serious threat to our environment. Water pollutants are usually produced by domestic, commercial, and industrial wastes.[1] Waste water contains organic (such as phenolic derivatives, polycyclic aromatic hydrocarbons, *etc.*)[2,3] and inorganic compounds, which can cause serious disorders for human as well animal and aquatic lives. Even very low concentrations of these pollutants can severely affect human health, so appropriate treatment of wastewater is required before disposing it into a river, canal, *etc.*

Photocatalysis is a prominent process for water purification utilizing solar energy. Many semiconductors are available for photocatalytic activity (*e.g.*, TiO_2,[4] ZnO,[5] and SnO_2,[6] *etc.*) for environmental remediation. TiO_2 is one of the most used materials because of its relatively low toxicity, low cost, high stability, strong oxidizing power, resistance to corrosion, and a wide spectrum of applications in food, paints, photocatalysts, photovoltaics, and sensors, *etc.*[7–11] TiO_2 is a well-known photocatalyst to degrade organic and inorganic pollutants such as methylene blue,[8] *para*-nitrophenol (4-NP),[12] phenol,[13] rhodamine-B,[14] potassium dichromate,[15] *etc.* over four decades. TiO_2 forms radicals ($OH^{\bullet}$) which are a most powerful oxidant to degrade a number of organic pollutant. However, TiO_2 still requires modifications with other nanomaterials because the excitons created under the UV light (femtosecond time scale) rapidly recombine in 10–100 nanosecond[16] and absorb only ultraviolet part of sun light due to wide bandgap (3.0–3.2 eV).[17] To improve the performance of TiO_2, hetero-structures were developed by utilizing metal deposition (Au, Ag, Pt, *etc.*),[18–20] binary composites with other metal oxide such as SnO_2,[21] conducting polymers such as polyaniline and non-metal doping

[a]*Department of Chemical Engineering and Center for Nanosciences, Indian Institute of Technology Kanpur, Kanpur – 208016, UP, India. E-mail: guptark@iitk.ac.in; Fax: +91-5122590104; Tel: +91-5122596972*

[b]*Center for Environmental Science and Engineering, Indian Institute of Technology Kanpur, Kanpur – 208016, UP, India*

† Electronic supplementary information (ESI) available: Element mapping and EDX analysis of CdS sensitized TiO_2 hollow, TiO_2 hollow and solid nanofibers, UV-Vis absorption spectra of different photocatalyst, BET, TGA, adsorption study with different photocatalyst, UV-Vis spectra of 4-NP with time, calibration curve of 4-AP and photocatalytic study under solar irradiation. See DOI: 10.1039/c6ra04305d

Open Access Article. Published on 26 April 2016. Downloaded on 7/28/2025 12:12:42 PM.
This article is licensed under a Creative Commons Attribution-NonCommercial 3.0 Unported Licence.

(N,[22,23] C,[24] S,[25] N/F[26] and B,[27] *etc.*). Such modifications of TiO_2 enhance its photocatalytic property due to either charge separation or increasing solar absorption or both. TiO_2 has been prepared by different methodologies such as hydrothermal,[28] electrospinning,[9,29] electrochemical,[30] *etc.* Various shaped nanostructures of TiO_2 have been developed such as nanoparticles,[31] nanooctahedra,[32] nanosheets,[33] hollow spheres,[34] nanofibers, and nanotubes,[4] *etc.* Charge separation and transportation of photogenerated excitons is another critical factor to improve photocatalytic efficiency. Staggered gap heterostructure is favourable for photocatalytic activity because electrons move to one semiconductor and holes move to the other.[35] To improve photocatalytic efficiency of TiO_2 in the visible range, heterostructures are prepared by sensitization with a narrow band gap semiconductor such as PbS,[36] CdSe,[37] CdS,[38] and CdTe,[39] *etc.* on TiO_2. Straddling gap type semiconductor heterostructures are formed when TiO_2 is sensitized with bulk PbS[40] and PbSe.[41,42] These restrict efficient electron transfer from PbS and PbSe to TiO_2 up to a certain size (<4.3 nm for PbS and <1 nm for PbSe).[43] Lin *et al.* prepared TiO_2 film by spin coating and then sensitized it with CdS and CdSe by the SILAR method and found that TiO_2/CdS heterostructure has higher electron transfer rate from CdS to TiO_2 than TiO_2/CdSe heterostructure.[44] Luo *et al.* prepared CdS and CdSe deposited TiO_2 nanotube array by hydrothermal and chemical vapour deposition and found that the TiO_2/CdS electrode had a lower recombination rate and higher chemical stability than TiO_2/CdSe.[45] Thus, sensitization of TiO_2 by CdS is an important modification due to its narrow band gap (2.4 eV) and its conduction band level being 0.5 eV more negative than the TiO_2 conduction band level.[46–48] Band alignment of TiO_2 and CdS (type-II heterostructure) favours photogenerated electrons transfer from the conduction band of CdS to the TiO_2 conduction band and holes transfer from the TiO_2 valence band to the CdS valance band.[46] Su *et al.* prepared TiO_2/CdS solid nanofibers through combining electrospinning with a hydrothermal process and found that the TiO_2/CdS structure shows excellent photocatalytic activity and visible light absorption.[49] Liu *et al.* prepared CdS sensitized TiO_2 film by microwave assisted chemical bath deposition and found that the reaction rate of CdS sensitized TiO_2 film was 8.4 times that of TiO_2 film for photocatalytic reduction of potassium dichromate.[38] Li *et al.* prepared TiO_2–CdS composite in aqueous medium and found that it helps to enhance visible light absorption and photocatalytic activity for the degradation of methylene blue.[50] Thus, sensitization of TiO_2 surfaces by CdS QDs has great importance for photocatalysis because of their increased visible light absorption and enhanced charge separation during photoreaction.

In this work, TiO_2 hollow nanofibers were prepared by a simple core shell electrospinning technique using mineral oil as core and TiO_2/polyvinylpyrrolidone (PVP) polymeric blend as the shell. High temperature calcination removes the carrier polymer PVP and thus produces mixed phase TiO_2 nanofibers whereas removal of mineral oil from the core creates hollow nanofibers. The as-synthesized hollow nanofibers were sensitized by CdS QDs through the SILAR method for different deposition cycles. CdS QDs are deposited easily on inner and outer surfaces of the nanofibers because of a hollow interior of the synthesized nanofibers. The hybrid TiO_2/CdS interfaces help in efficient charge separation and enhanced light absorption owing to quantum confinement. We also demonstrated the efficacy of the electrospun solid and hollow TiO_2 nanofibers towards efficient photocatalytic degradation of 4-NP dye. Further, the effect of CdS QDs sensitization over hollow TiO_2 nanofibers towards enhanced photocatalytic degradation of the same dye is also demonstrated.

2. Experimental section

2.1. Materials

Titanium tetra isopropoxide (TTIP, 97%), cadmium nitrate tetrahydrate ($Cd(NO_3)_2 \cdot 4H_2O$), 4-NP and sodium borohydride ($NaBH_4$) were purchased from Sigma-Aldrich. Sodium sulphide (Na_2S) and PVP (M_w = 1 300 000) were purchased from Alfa Aesar. Ethanol, acetic acid, and methanol were purchased from Merck. Mineral oil was purchased from Loba chemicals. All the chemicals were used as received.

2.2. Synthesis of TiO_2 hollow nanofibers

TTIP was used as a titania source. Solution (A) was prepared by mixing 3 g TTIP in 6 mL ethanol and 6 mL acetic acid. This was stirred at room temperature for 20–25 min. Solution (B) was prepared by mixing of 0.90 g PVP in 15 mL ethanol at 55 °C for 20–30 min in a capped bottle. Both solutions (A and B) were mixed in glass bottle and stirring was continued for 8 h at room temperature to get a homogeneous solution for electrospinning. The prepared electrospun solution was loaded in a 10 mL plastic syringe on the shell side while the core side fluid was mineral oil (heavy). Flow rate of core and shell side fluids were fixed at 8 and 12 μL min^{-1}, respectively, while the distance and high voltage applied between syringe needle and collector were 10 cm and 12 kV, respectively. The nanofibers mat was collected on a rotary drum over aluminium foil. In a subsequent step, the nanofibers mat was calcined inside a muffle furnace with a ramp rate 5 °C min^{-1} and kept at 500 °C for 2 h to remove polymer and mineral oil completely. Fig. 1a shows the schematic diagram of the electrospinning setup. For preparation of solid nanofibers, core solution (mineral oil) was replaced with an electrospun solution of titania.

2.3. CdS sensitization on hollow TiO_2 nanofibers

As shown in Fig. 1b, TiO_2 hollow nanofibers were sensitized by CdS QDs using a successive ion layer adsorption and reaction (SILAR) method. TiO_2 hollow nanofibers were first immersed in 0.05 M $Cd(NO_3)_2 \cdot 4H_2O$ solution in ethanol for 5 min, followed by washing with ethanol and drying with a N_2 gun. Then in subsequent steps, the hollow nanofibers mat was immersed in 0.05 M Na_2S solution in methanol for 5 min, followed by washing with methanol and drying with a N_2 gun; this completed one cycle. The cycle was repeated several times for different CdS QDs loading.

 This journal is © The Royal Society of Chemistry 2016

Open Access Article. Published on 26 April 2016. Downloaded on 7/28/2025 12:12:42 PM.
This article is licensed under a Creative Commons Attribution-NonCommercial 3.0 Unported Licence.

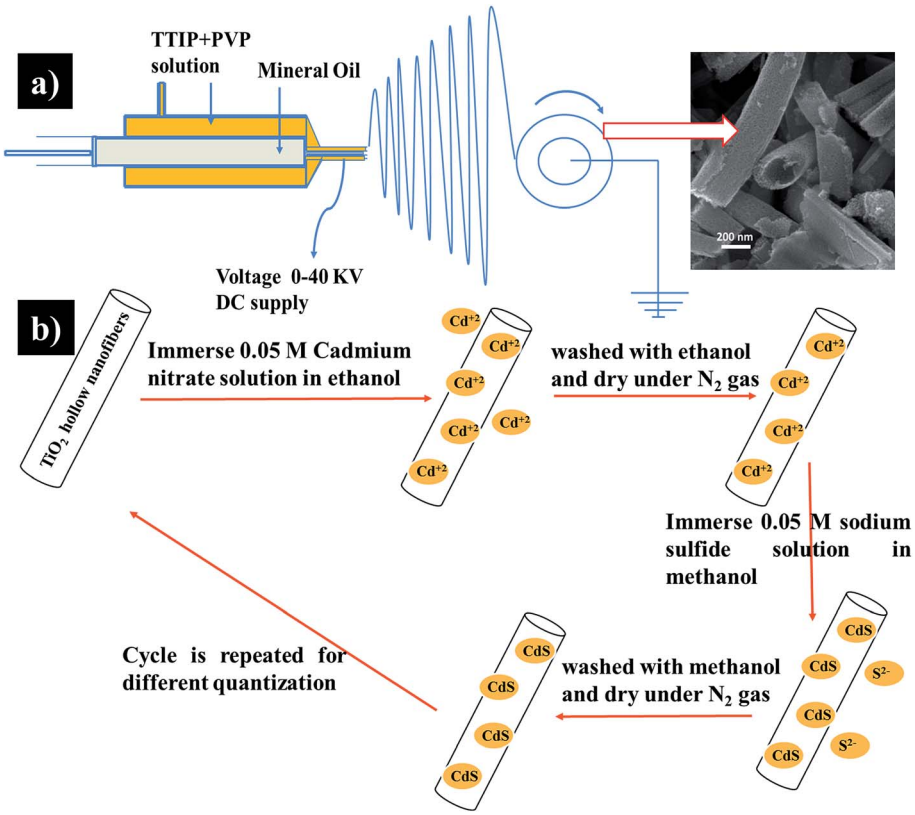

Fig. 1 Schematic diagram of (a) electrospinning setup for preparation of TiO_2 hollow nanofibers and (b) CdS QDs sensitization over hollow nanofibers by SILAR route.

2.4. Photocatalytic experiments

0.01 M 4-NP and 0.01 M $NaBH_4$ solutions were prepared in deionized (DI) water. 100 μL of freshly prepared 10^{-2} M 4-NP solution was mixed with freshly prepared 10 mL of $NaBH_4$ solution resulting in 4-NP solution concentration of 10^{-4} M. Different amounts of photocatalyst (1–10 mg mL^{-1}) were added in the pollutant (4-NP solution) to study the loading effect. A comparative study of different photocatalyst was carried out with 1 mg mL^{-1} of photocatalyst to 4-NP solution. The 4-NP solution was exposed under UV light (365 nm, 1.07 mW cm^{-2}) in the presence of photocatalyst. At different time intervals, absorption of 4-NP was measured using a UV-Vis absorption spectrophotometer. Adsorption of different photocatalysts was studied separately with the same photocatalyst loading as used for comparative studies.

2.5. Characterization

Micrographs of solid, hollow, and CdS sensitized hollow nanofibers were captured by a field emission scanning electron microscope (FESEM, Quanta 200, Zeiss, Germany) and transmission electron microscope (TEM, Tecnai 20 G^2 STWIN, USA). High resolution transmission electron microscope (HRTEM) micrographs were imaged with a 200 kV JEOL JEM-2010 (Japan). The TEM sample was prepared by dispersing 2 mg sample in 2 mL of ethanol through sonication followed by loading of 1–2 drops over a carbon coated TEM grid and dried overnight to remove solvent. The crystal structures of prepared TiO_2 solid, hollow and TiO_2/CdS nanofibers were investigated by X-ray diffraction (XRD, X'Pert Pro, PANanalytical, Netherlands) using Cu Kα radiation (λ = 1.5406 Å). Raman spectra were collected on a Raman spectrometer (WiTec, Germany using laser light of 532 nm wavelength). Surface area and pore size distribution of prepared nanofibers were investigated by Brunauer–Emmett–Teller theory (BET, Quantachrome Instruments, USA). Further element detection and element mapping were carried out using energy dispersive X-ray spectroscopy (EDX linked to FESEM, Oxford Instrument, UK). Thermal behaviour of the as-spun nanofibers mat was analysed by thermogravimetric analysis (TGA, TA instrument, USA). UV-Vis absorption spectra of all photocatalysts were recorded by Varian Cary 50 Bio UV-Vis Spectrophotometer (USA). Absorbance of 4-NP at 400 nm was probed by the same UV-Vis instrument at different times.

3. Results and discussion

3.1. Morphological analysis

Fig. 2a shows a FESEM micrograph of annealed partially aligned TiO_2 solid nanofibers which are continuous and distributed evenly throughout the matrix. The diameters of solid nanofibers are in the range of 100–140 nm (diameter distribution of nanofibers into matrix is shown in Fig. 2a) and an average diameter of the nanofibers is ~125 nm. The length of prepared

Open Access Article. Published on 26 April 2016. Downloaded on 7/28/2025 12:12:42 PM.
This article is licensed under a Creative Commons Attribution-NonCommercial 3.0 Unported Licence.

solid nanofibers is of several μm as observed from Fig. 2a. TiO_2 solid nanofibers are found to be smooth in nature. To get further insights of TiO_2 solid nanofibers morphology, a TEM image of solid nanofibers is shown in Fig. 2c, which confirms their solid nature and resembles those with FESEM micrograph. Fig. 2b shows FESEM images of annealed electrospun hollow nanofibers which are hollow in nature (shown by oval in Fig. 2b). Hollow nanofibers diameters, as observed by a micrograph, are in the range of 80–140 nm (diameter distribution into matrix is shown in Fig. 2b), an average diameter is ~120 nm, and they have lengths of several μm. The surface of the nanofibers appears porous in nature. In order to further analyse the microstructure of TiO_2 hollow nanofibers, TEM was carried out. Fig. 2d shows a TEM micrograph which confirms the porous and hollow nature of nanofibers as observed in FESEM. Pore size distribution was investigated by BET and will be discussed in a later section. Some broken hollow nanofibers are also shown in micrographs which confirmed their hollow nature. Element detection and mapping of solid and hollow nanofibers are shown in Fig. S1 and S2;† they show presence of Ti and O atoms only, which means the complete removal of polymer and solvent during the calcination step.

CdS QDs were deposited over nanofibers by the SILAR method. TiO_2 nanofibers first adsorbed Cd^{2+} ions when immersed in an ethanolic solution of $Cd(NO_3)_2 \cdot 4H_2O$. Then in the next step, these were washed with ethanol solution to remove excess Cd^{2+} ions from the TiO_2 hollow nanofibers. Cd^{2+} ions adsorbed TiO_2 hollow nanofibers were then immersed in Na_2S solution. Reaction between Cd^{2+} and S^{2-} ions resulted in CdS formation onto TiO_2 nanofibers. CdS deposition could be controlled by concentration of precursor ions, time, and number of cycles. In this work, we fixed the precursor concentration and time of each cycle and varied the number of SILAR cycles. CdS loading on TiO_2 hollow nanofibers was increased with increase in the SILAR cycle, as confirmed by EDX (Fig. S1†). Fig. 3a–d show FESEM micrographs of CdS QDs sensitized TiO_2 hollow nanofibers after 1, 2, 3, and 5 SILAR cycles. From the micrographs, it can be observed that the nanofibers matrix does not lose its hollow morphology, as seen earlier for TiO_2 hollow nanofibers (shown by oval in Fig. 3a–d). Apart from the hollow nature of nanofibers, the micrographs clearly indicate a porous nature. To get further insight of the CdS sensitized TiO_2 hollow nanofibers, TEM micrographs were taken as shown in Fig. 3e–h which confirms the porous and hollow nature of them. TEM micrographs also show that the surface of CdS sensitized TiO_2 hollow nanofibers is rough in nature. Element mapping for CdS sensitized TiO_2 hollow nanofibers after 1, 2, 3, 5, and 10 cycles is shown in Fig. S3† and shows that CdS is evenly distributed throughout the matrix. A more detailed microstructure analysis of nanofibers was carried out using HRTEM. TiO_2 solid nanofibers showed they contain the anatase phase plane (101) with lattice spacing of 0.352 nm as shown in Fig. 4a. TiO_2 hollow nanofibers microstructure (Fig. 4b) contains one additional rutile phase plane (200) with lattice spacing of 0.192 nm. CdS sensitized TiO_2 hollow nanofibers after 2 and 5 cycles are shown in Fig. 4c and d, respectively. HRTEM images contain additional (100) plane of CdS with lattice spacing of 0.359 nm. Size of QDs varies with SILAR cycles. The size of CdS QDs onto TiO_2 hollow nanofibers is 3–4 nm after 2 cycles and increases to 4–6 nm after 5 cycles.

3.2. Phase analysis

To get the crystalline information of synthesized materials, XRD patterns of electrospun solid, hollow, and CdS sensitized hollow

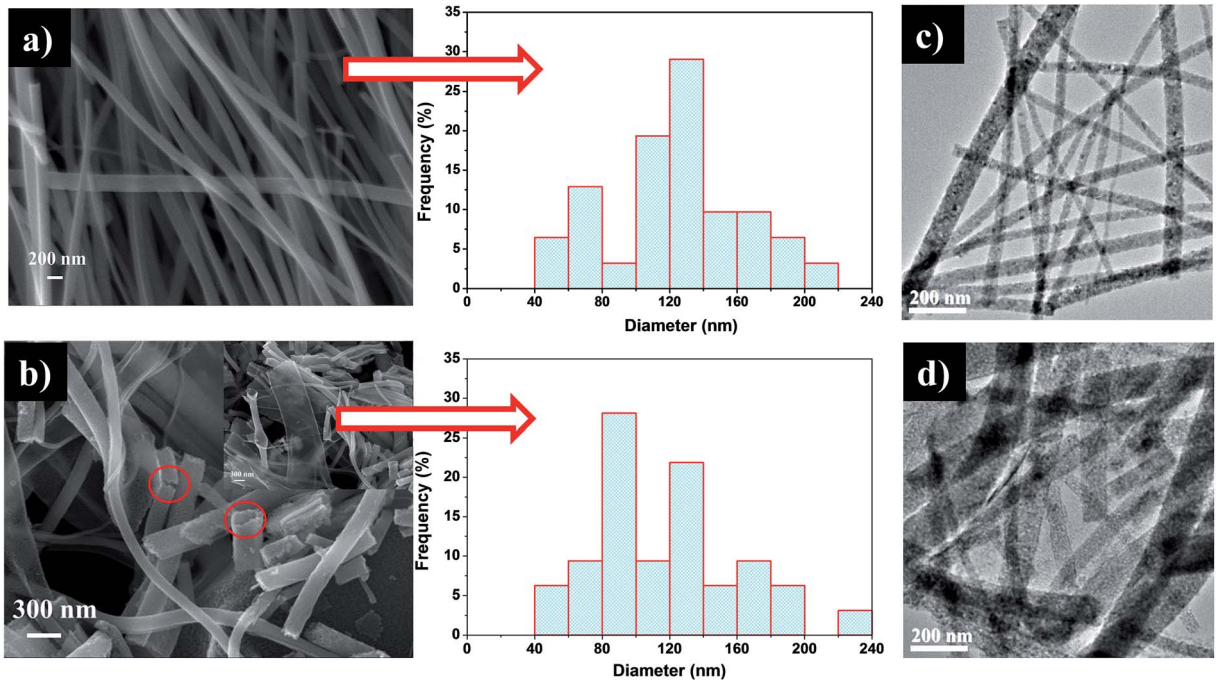

Fig. 2 FESEM micrographs and size distribution histogram of (a) TiO_2 solid nanofibers, (b) TiO_2 hollow nanofibers (encircled shows hollow morphology of nanofibers); TEM images of (c) TiO_2 solid nanofibers, (d) TiO_2 hollow nanofibers.

 This journal is © The Royal Society of Chemistry 2016

Open Access Article. Published on 26 April 2016. Downloaded on 7/28/2025 12:12:42 PM.
This article is licensed under a Creative Commons Attribution-NonCommercial 3.0 Unported Licence.

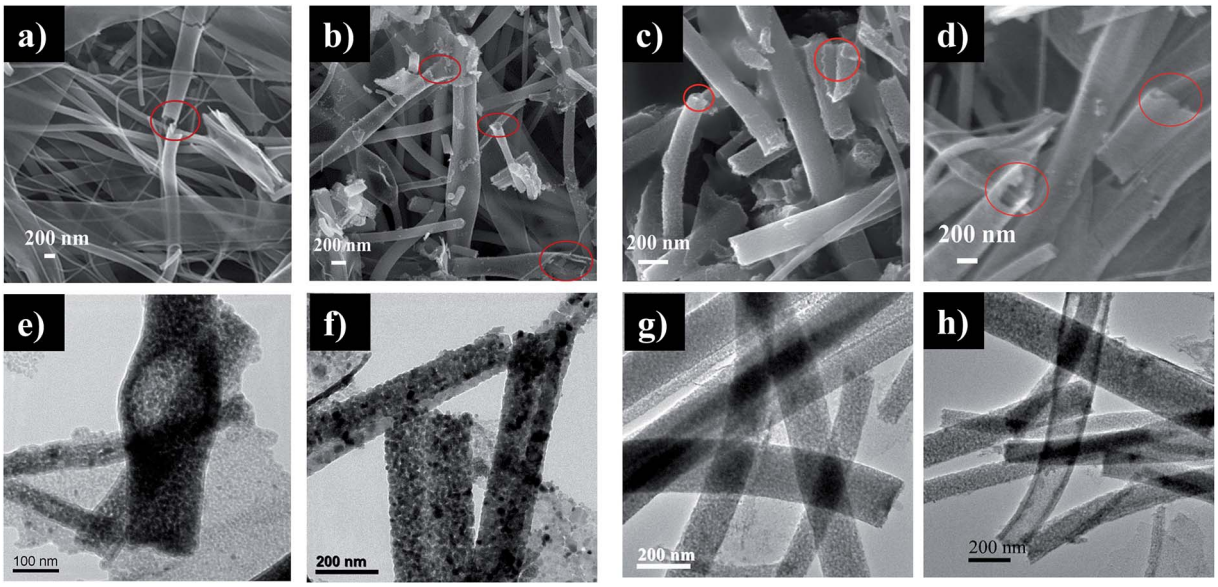

Fig. 3 FESEM micrographs (a, b, c, and d) of CdS loaded TiO_2 hollow nanofibers after 1, 2, 3, and 5 SILAR cycles, respectively (encircled shows hollow morphology of nanofibers); TEM images (e, f, g, and h) of CdS loaded TiO_2 hollow nanofibers after 1, 2, 3, and 5 SILAR cycles, respectively.

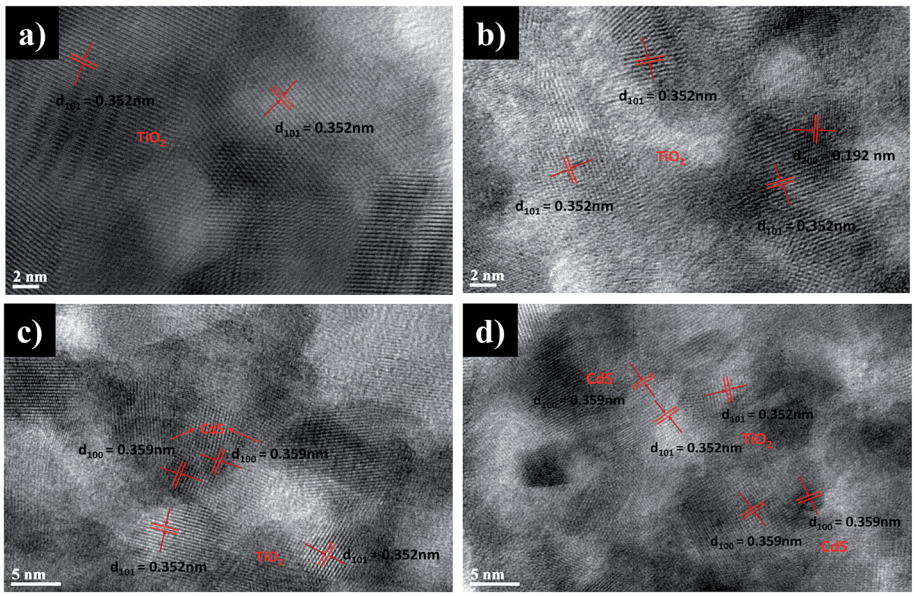

Fig. 4 High resolution TEM images of (a) TiO_2 solid nanofibers, (b) TiO_2 hollow nanofibers, (c) and (d) CdS sensitized TiO_2 hollow nanofibers after 2 and 5 SILAR cycles, respectively.

nanofibers of TiO_2 were recorded as shown in Fig. 5a. For solid and hollow nanofibers, there are no diffraction peaks corresponding to organic compounds which confirm complete removal of polymer and mineral oil during calcination. Solid nanofibers contain much less rutile phase while hollow nanofibers of TiO_2 contain mixed crystalline phases of rutile and anatase. The sharp peaks at 2θ values of 25.30°, 37.87°, 48.00°, 54.33°, 55.08°, and 62.73° are well matched with characteristic peaks of (101), (004), (200), (105), (211), and (204) planes of the anatase phase of TiO_2, respectively (PCD 1627926), and peaks at 2θ values of 27.42°, 36.06°, 41.28°, 44.06°, and 56.57 are matched with characteristic peaks of (110), (101), (111), (210), and (220) planes of the rutile phase of TiO_2, respectively (PCD 1714347). There are no other peaks found in the XRD pattern other than anatase and rutile confirming mixed phases of TiO_2 with high purity. Further XRD patterns of CdS sensitized TiO_2 hollow nanofibers were evaluated and it was found that some additional peaks appeared at 2θ values of 26.25°, 43.9°, and 51.97° which are assigned to planes (002), (110), and (112), respectively of deposited hexagonal wurtzite phase of CdS (PCD 1410956). Loading of CdS on TiO_2 was increased with an increase in SILAR cycles as confirmed through stronger peaks of

Open Access Article. Published on 26 April 2016. Downloaded on 7/28/2025 12:12:42 PM.
This article is licensed under a Creative Commons Attribution-NonCommercial 3.0 Unported Licence.

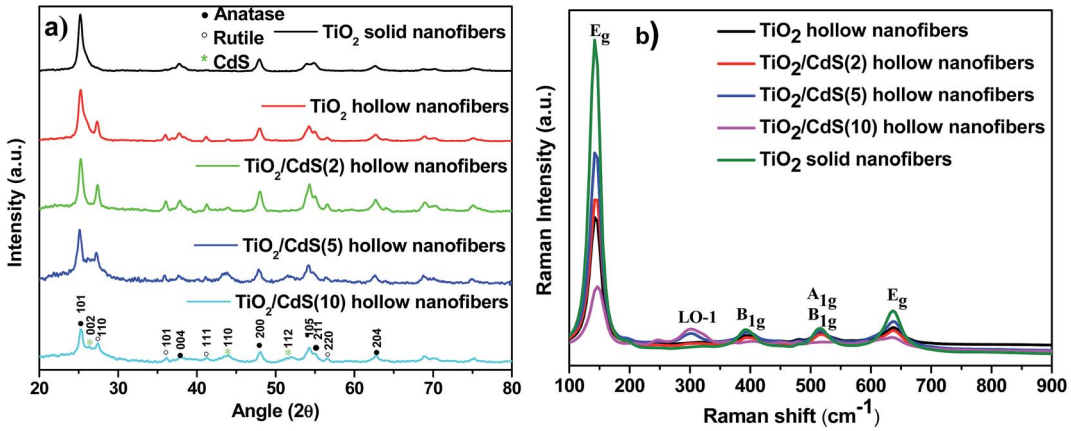

Fig. 5 (a) XRD pattern and (b) Raman spectra of solid, hollow, and CdS sensitized hollow TiO_2 nanofibers; number in the parentheses denotes number of SILAR cycles.

CdS. The XRD patterns suggest that the CdS sensitized TiO_2 hollow nanofibers are heterostructures with the three phase structure of anatase TiO_2, rutile TiO_2, and hexagonal wurtzite phase of CdS.

3.3. Raman, BET, UV-Vis spectra and TGA

To analyse the structural characteristics of TiO_2 solid and TiO_2 hollow nanofibers, Raman spectroscopy was recorded in the range of 36–3780 cm^{-1}. The Raman spectra of nanofibers and sensitized nanofibers are shown in Fig. 5b (range 100–900 cm^{-1}). The first E_g peak at 144 cm^{-1} is a characteristic peak of anatase TiO_2. The peaks at 640 cm^{-1} and 517 cm^{-1} correspond to E_g, $A_{1g} + B_{1g}(2)$ modes of anatase TiO_2, respectively. The peak at 396 cm^{-1} is assigned to the $B_{1g}(1)$ mode and the main peak at 144 cm^{-1} corresponds to the E_g vibrational mode.[4] The Raman spectrum of CdS sensitized TiO_2 hollow nanofiber is shown in Fig. 5b. CdS sensitized TiO_2 hollow nanofibers contain all characteristic peaks of TiO_2 hollow nanofibers along with an additional peak at 300 cm^{-1} which matches with the longitudinal optical phonon mode (LO-1) of bulk CdS[51] this peak becomes stronger as CdS loading increases.

The surface area and porosity of prepared TiO_2 solid and hollow nanofibers were investigated by N_2 adsorption and desorption isotherms. Fig. S4b† shows the N_2 adsorption–desorption isotherm of the as-prepared calcined TiO_2 hollow nanofibers. It shows a type IV-like isotherm shape according to the IUPAC classification,[52] which indicates presence of mesoporous material. Fig. S4a† shows the pore size distribution plot determined by the BJH (Barrett–Joyner–Halenda) method, which shows that the pore size of TiO_2 hollow nanofibers is in the range of mesoporous materials while some macropores are also present having a pore size less than 110 nm. Total pore volume and BET surface area of TiO_2 hollow nanofibers are 0.1144 $cm^3\ g^{-1}$ and 34.89 $m^2\ g^{-1}$, respectively. The microporous, mesoporous, and macroporous volume in TiO_2 hollow nanofibers are 0.0040, 0.0999, and 0.0105 $cm^3\ g^{-1}$, respectively. TiO_2 hollow nanofibers are mesoporous dominant with 87.30% volume of the total pore volume. Fig. S4c and d† show pore size distribution and N_2 adsorption and desorption curves of TiO_2 solid nanofibers. Total pore volume and BET surface area of TiO_2 solid nanofibers are 0.046 $cm^3\ g^{-1}$ and 17.42 $m^2\ g^{-1}$, respectively. It contains both mesopores and macropores, having more mesopores with 76.78% of the total pore volume.

UV-Vis absorption spectra of different photocatalysts are shown in Fig. S5,† which indicate that the TiO_2 solid and hollow nanofibers are only active in the UV light region. The absorbance peaks appear at 332 nm and 326 nm for TiO_2 solid nanofibers and TiO_2 hollow nanofibers, respectively. The absorption edge of TiO_2 solid and hollow nanofibers is around 390 nm. CdS sensitized TiO_2 hollow nanofibers show some additional variable absorption along with absorption peaks of TiO_2 hollow nanofibers. Absorption spectra of CdS sensitized TiO_2 hollow nanofibers after 1 and 2 SILAR cycles show broadened absorption peaks in the UV range; when QDs deposition was increased with 3, 5, and 10 SILAR cycles, additional absorption was found in the range of 390–500 nm. Colour of the material changes from white to light yellow followed by dark yellow with increasing SILAR cycles (inset of Fig. S5†). There is a redshift with increased loading of CdS, as shown in Fig. S5,† due to quantum confinement.

Fig. S6† (dotted line) shows a TGA curve of as-spun hollow nanofibers. It can be represented as a three step process and total weight loss of 95.72% occurred during the calcination process. In the first step, when temperature was increased from room temperature to 220 °C, weight loss of 3.2% was observed due to desorption of solvent and water. In the second step, when temperature was increased from 220 °C to 350 °C, there was a major weight loss (66%) due to removal of mineral oil and may be some polymer. In the last step, with temperature changed from 350 °C to 490 °C, a weight loss of 26.5% was due to removal of organic polymer. Further increment of temperature did not cause any weight loss. These results show that polymer and mineral oil are completely decomposed up to 490 °C which was confirmed by EDX and XRD earlier as well. Total weight loss during calcination of as-spun TiO_2 solid nanofibers was 66.70% due to removal of solvent and polymer (Fig. S6† continuous line).

 This journal is © The Royal Society of Chemistry 2016

Open Access Article. Published on 26 April 2016. Downloaded on 7/28/2025 12:12:42 PM.
This article is licensed under a Creative Commons Attribution-NonCommercial 3.0 Unported Licence.

3.4. Photocatalytic studies

Photocatalytic experiments were performed in a petridish under UV light in the presence of the photocatalyst. In the presence of $NaBH_4$, the yellow colour solution of 4-NP turns dark yellow indicating presence of phenolate ion. Presence of phenolate ion was also confirmed by UV-Vis absorption spectra because a 4-NP peak shifted from 317 nm to 400 nm.[53] TiO_2 nanofibers convert 4-NP photocatalytically into a useful product, *para*-aminophenol (4-AP), which is an intermediate for the preparation of medicines like paracetamol. A further adsorption study of 4-NP was done on solid, hollow, and QDs sensitized hollow TiO_2 nanofibers under dark conditions. The 4-NP concentration after 4 h was decreased by ~13%, 19%, and 9% for solid, hollow, and QDs sensitized hollow TiO_2 nanofibers, respectively as shown in Fig. S7.† It has been observed that the adsorption process does not dominate during photocatalyst test under UV light.

Further, we investigated the effect of photocatalyst loading of TiO_2 hollow nanofibers on photocatalytic performance. Photocatalyst loading was varied from 1–10 mg mL^{-1} of 10^{-4} M 4-NP in the presence of 10^{-2} M $NaBH_4$ and the solution was exposed under UV light. The yellow colour of the 4-NP solution gradually vanished and thus confirmed the occurrence of a photocatalytic reaction. A small peak appears at 300 nm as the photocatalytic reaction proceeds indicating the formation of 4-AP[53] which gradually increased with time. The photodegradation of 4-NP can be defined as a pseudo first order reaction as given in eqn (1),

$$-\frac{dC}{dt} = KC \quad (1)$$

where C is concentration of 4-NP, K is the pseudo first order rate constant and t is illumination time. The integration of eqn (1) gives:

$$\ln\left(\frac{C_o}{C}\right) = Kt \quad (2)$$

where C_o is the initial concentration of 4-NP. The pseudo first order rate constant was calculated from the concentration time profile of 4-NP. Fig. 6a shows the concentration profile of 4-NP with illumination time. Here, it was observed from Fig. 6b and Table 1 that the rate constant does not increase with the same ratio as loading is increased due to mass transfer and light absorption limitation. Even when photocatalyst loading is increased by 10 times, the rate constant only increases by 4.9 times. In spite of these limitations, the rate constant of the photocatalytic reaction increases with increasing photocatalyst loading.

To compare the performance of different photocatalysts, we performed experiments for 4-NP degradation with different photocatalysts. As time increased, the yellow colour of 4-NP weakened which implies the photocatalytic degradation of 4-NP into 4-AP. UV-Vis absorption spectra of 4-NP with irradiance time is shown in Fig. S8† in presence of TiO_2 solid nanofibers, TiO_2 hollow nanofibers, and TiO_2/CdS(3) hollow nanofibers. The evolution of concentration ratio (C/C_o) with exposure time is shown in Fig. 7a. It is observed that TiO_2 hollow nanofibers show 2.2 times better photocatalytic activity than the solid one. This is due to the hollow and mesoporous nature of nanofibers. Another possible reason for increased photocatalytic activity might be due to multi-light scattering/reflection, which might have enhanced light harvesting.[54,55] We also tested the photocatalytic activity of CdS sensitized TiO_2 hollow nanofibers. From Fig. 7a, it was observed that photocatalytic activity significantly improved with CdS QDs sensitization. As we increased the CdS QDs loading on TiO_2 hollow nanofibers, photocatalytic activity improved significantly for 1, 2, and 3 SILAR cycles. However, photocatalytic activity decreased for 5 and 10 SILAR cycles in comparison to 3 SILAR cycles. Decrease in photocatalytic activity for 5 and 10 SILAR cycles may be due to increase in average distance between CdS and TiO_2 resulting in contact losses and loss of pores due to higher loading of CdS.[56–58] At low CdS loading, photocatalytic activity of CdS QDs sensitized TiO_2 hollow nanofibers enhances due to more hot catalytic spots between TiO_2 and CdS which act as charge separation centers.[59] Under UV light exposure, TiO_2 and CdS both create excitons (electron–hole pair). CdS transfers electrons from the conduction band of CdS to the TiO_2 conduction band and similarly, holes are transferred from the TiO_2 valance band to the CdS valance band. For the photocatalytic reduction of 4-NP, a pseudo first order kinetic rate constant was calculated from

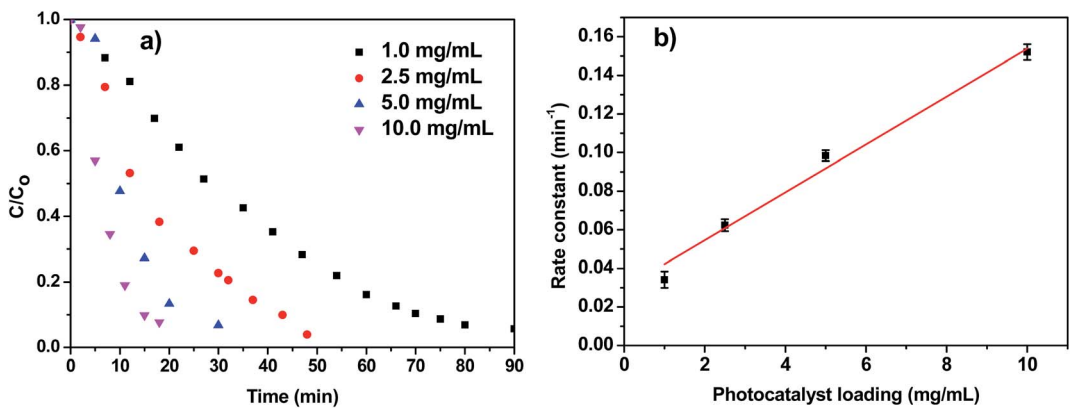

Fig. 6 (a) Photocatalytic activity of TiO_2 hollow nanofibers for 4-NP degradation under UV light with different loading (mg of photocatalyst per mL of 10^{-4} M 4-NP), (b) rate constant values for different photocatalyst loading.

Open Access Article. Published on 26 April 2016. Downloaded on 7/28/2025 12:12:42 PM.
This article is licensed under a Creative Commons Attribution-NonCommercial 3.0 Unported Licence.

Table 1 Rate constants with photocatalyst loading (mg of photocatalyst per mL of 4-NP solution) of TiO_2 hollow nanofibers

Photocatalyst loading	Rate constant (min^{-1})
1 mg mL^{-1}	0.0312 ± 0.0043
2.5 mg mL^{-1}	0.0623 ± 0.0031
5 mg mL^{-1}	0.0984 ± 0.0028
10 mg mL^{-1}	0.1520 ± 0.0041

$\ln(C_o/C)$ *vs.* time graph (Fig. 7b). The pseudo first order rate constant of CdS sensitized TiO_2 hollow nanofibers after 3 SILAR cycles was 7.7 and 3.5 times higher than solid and hollow TiO_2 nanofibers, respectively. The pseudo first order kinetic rate constants of different photocatalysts follow the order: TiO_2/CdS(3) > TiO_2/CdS(2) > TiO_2/CdS(1) > TiO_2/CdS(5) > TiO_2/CdS(10) > TiO_2 hollow nanofibers > TiO_2 solid nanofibers (Table 2). Competitive removal due to adsorption and photocatalysis was shown in Fig. 7c for different photocatalysts for 25 min duration. It was observed that adsorption did not have a significant contribution towards removal of 4-NP in comparison to photocatalytic activity. 4-AP concentration was calculated at the end of the reaction using a calibration curve (Fig. S9†) and the conversion rate was estimated to be 81.2%, 90.1%, 90.3%, 90.1%, 90.5%, 89.9%, and 90.1% for the TiO_2 solid nanofibers, TiO_2 hollow nanofibers, TiO_2/CdS(1), TiO_2/CdS(2), TiO_2/CdS(3), TiO_2/CdS(5), and TiO_2/CdS(10) hollow nanofibers photocatalyst, respectively. We also demonstrated the photocatalytic activity of TiO_2 hollow nanofibers and TiO_2/CdS(3) hollow nanofibers under solar light and found that TiO_2/CdS(3) hollow nanofibers had 47 times more photocatalytic activity than the TiO_2 hollow nanofibers (Fig. S10†). The increase in photocatalytic activity is due to efficient charge separation as well as enhanced visible light absorption.

Reusability of TiO_2 hollow nanofibers was investigated under UV light irradiance with 5 mg of TiO_2 hollow nanofibers per mL solution of 10^{-4} M 4-NP. Results are shown in Fig. 7d for 3 cycles of reuse. The photocatalyst does not need any regeneration step for the successive reusability test and its photocatalytic activity does not change significantly in successive reusable cycles. FESEM micrograph (Fig. 7d inset) was taken after reuse and it was observed that TiO_2 nanostructures did not change significantly even after 3 cycles of reuse.

The proposed mechanism of photocatalytic degradation of 4-NP is shown in Fig. 8a. In CdS QDs sensitized TiO_2, the excitons are generated in TiO_2 and CdS under UV light irradiance. It has already been mentioned earlier that the conduction band of TiO_2 is situated below the conduction band of CdS. As a result, the photogenerated electrons in the conduction band of CdS can be easily transferred to the conduction band of TiO_2 while holes remain in the CdS valance band. Exciton separation can be easily enhanced in the heterostructure and significantly improves photocatalytic

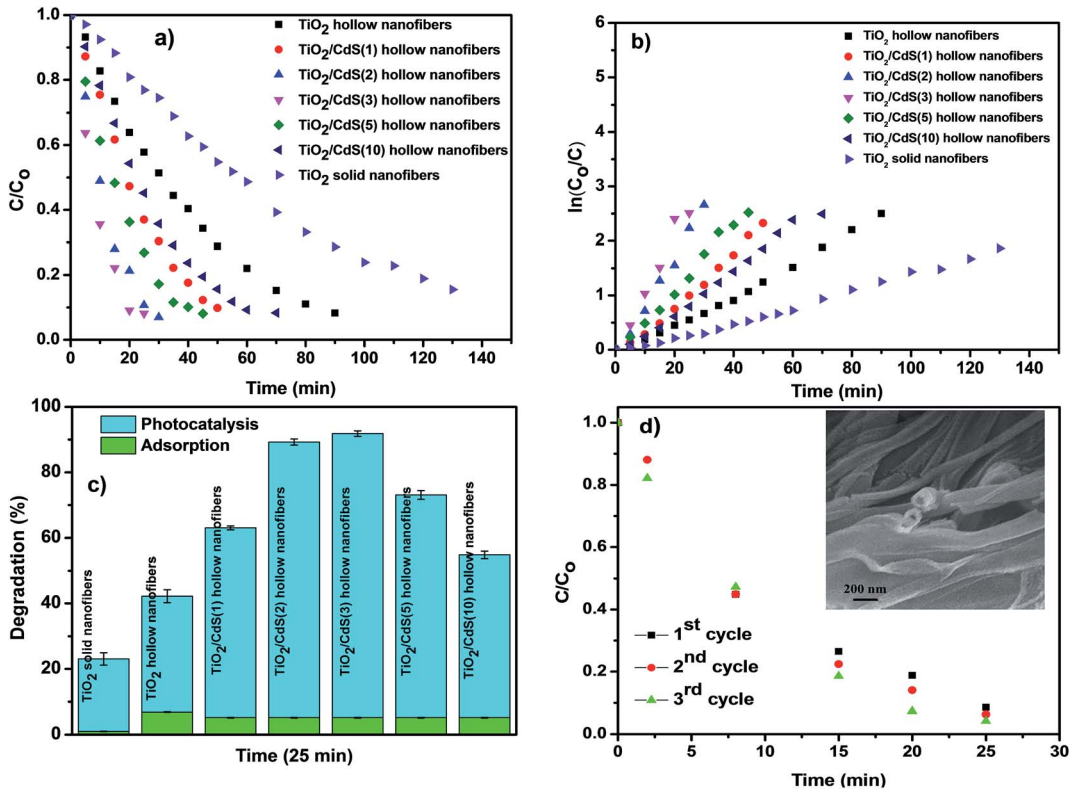

Fig. 7 (a) Photocatalytic activity of solid, hollow, and CdS sensitized hollow TiO_2 nanofibers for degradation of 4-NP in presence of $NaBH_4$ (photocatalyst loading = 1 mg mL^{-1} of 10^{-4} M 4-NP), (b) photocatalytic reaction kinetics of 4-NP with reaction time, (c) competitive removal due to adsorption and photocatalytic activity for 25 min, (d) photocatalytic activity of TiO_2 hollow nanofibers tested for 3 cycles (loading 5 mg of TiO_2 hollow nanofibers per mL of 10^{-4} 4-NP); inset shows FESEM micrograph TiO_2 hollow nanofibers after 3 cycles of reusability test.

This journal is © The Royal Society of Chemistry 2016

Open Access Article. Published on 26 April 2016. Downloaded on 7/28/2025 12:12:42 PM.
This article is licensed under a Creative Commons Attribution-NonCommercial 3.0 Unported Licence.

Table 2 Rate constants with different photocatalysts

Photocatalyst (1 mg mL^{-1} of 10^{-4} M 4-NP)	Rate constant (min^{-1})
TiO_2 hollow nanofibers	0.0312 ± 0.0043
TiO_2/CdS(1) hollow nanofibers	0.0479 ± 0.0025
TiO_2/CdS(2) hollow nanofibers	0.0862 ± 0.0064
TiO_2/CdS(3) hollow nanofibers	0.1078 ± 0.0054
TiO_2/CdS(5) hollow nanofibers	0.0592 ± 0.0048
TiO_2/CdS(10) hollow nanofibers	0.0392 ± 0.0038
TiO_2 solid nanofibers	0.0140 ± 0.0009

efficiency. Separated holes take part in the reaction with water to convert into H^+ ions and OH free radicals intermediates. The conversion of 4-NP to 4-AP reduction scheme is presented in Fig. 8a.[60] The $6H^+$ and $6e^-$ take part in the photocatalytic conversion of 4-NP to 4-AP in the presence of photocatalyst. Electrons are provided by the photocatalyst material under light irradiance,[61] while H^+ are provided from the aqueous $NaBH_4$ solution.[62] 4-NP is converted to 4-nitrosophenol, followed by conversion to 4-hydroxyaminophenol, and finally converted to 4-AP in the presence of photocatalyst with $NaBH_4$ solution under UV light irradiance (Fig. 8a). Only 4-AP is observed as a final product after reaction. Digital images of 4-NP (before reaction) and 4-AP (after reaction) are shown in Fig. 8b.

4. Conclusions

We have demonstrated the synthesis of mixed phase TiO_2 hollow nanofibers by coaxial electrospinning. The as-prepared TiO_2 hollow nanofibers were thereby sensitized with CdS QDs by the SILAR method. The CdS QDs sensitized TiO_2 nanofibers were found to have significantly enhanced light absorption as compared to pristine TiO_2 nanofibers. Photocatalytic activities of the electrospun hollow TiO_2 and TiO_2/CdS nanofibers were evaluated for degradation of 4-NP dye. The nanofibers preserved their structural morphology and activity after repetitive photocatalytic usage. Photocatalysts showed pseudo first order kinetics for the degradation of 4-NP under UV light and degradation was enhanced significantly through sensitization with QDs. The photocatalytic activity of TiO_2/CdS(3) was found to be ~3 times more efficient than hollow TiO_2 nanofibers and ~8 times effective than the solid nanofibers. The improved photocatalytic activity is the result of enhanced absorption and efficient electron–hole separation for TiO_2/CdS nanofibers. These materials could further find applications for

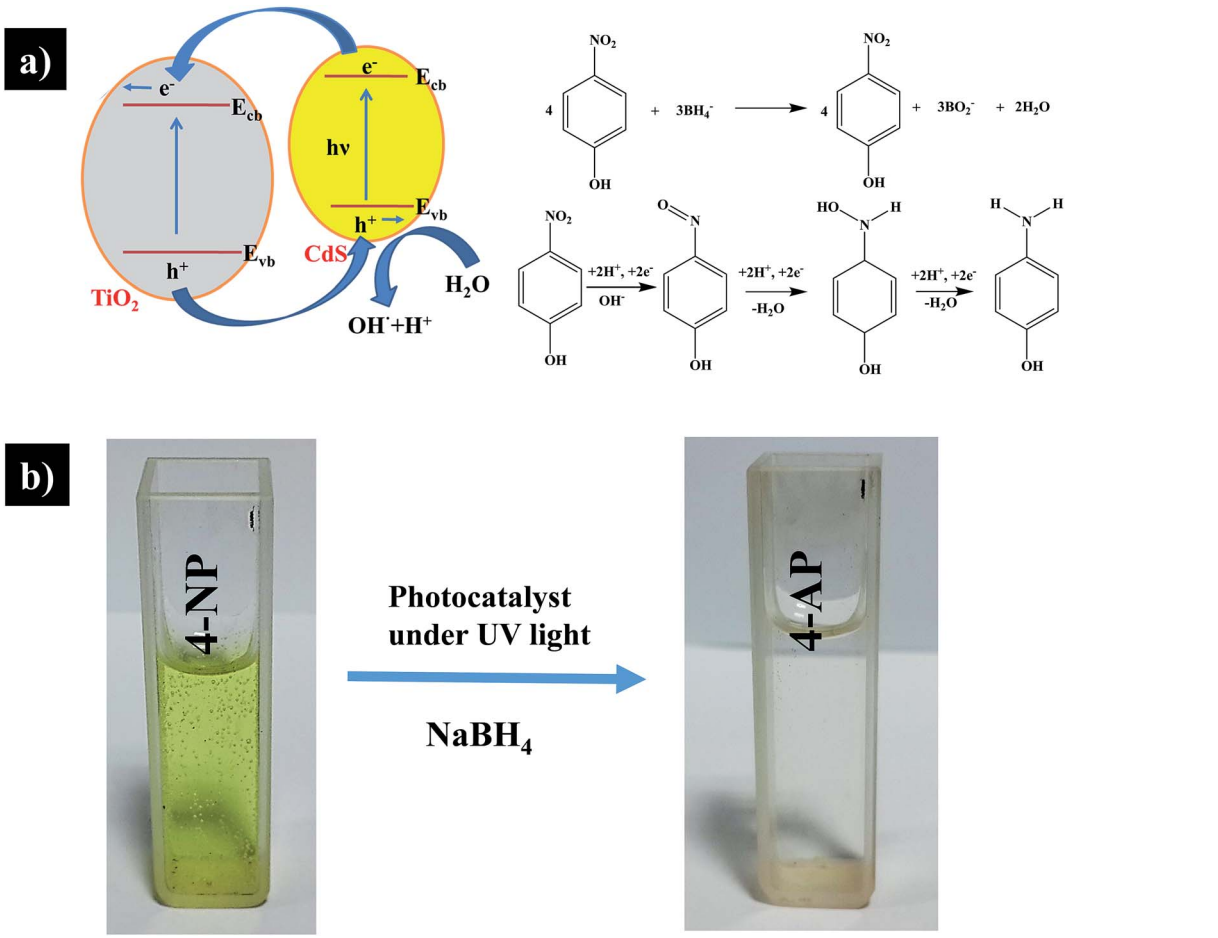

Fig. 8 (a) Schematic illustration for photocatalytic degradation mechanism on CdS/TiO_2 under UV light irradiance and (b) digital image of 4-NP and 4-AP solution.

photocatalytic water splitting, dye sensitized solar cells, Li-ion batteries, supercapacitor electrodes, and sensors.

Acknowledgements

RKG acknowledges financial assistance from Department of Science and Technology (DST), India INSPIRE Faculty Award (Project No. IFA-13 ENG-57) and Indian Institute of Chemical Engineers (IIChE) (Project No. AKD/R&D/2013/15152). DST support is acknowledged to the Center for Nanosciences. Authors are thankful to Prof. P. V. Satyam of Institute of Physics, Bhubaneswar, Odisha for helping in HRTEM characterization.

References

1 H. Park, Y. Park, W. Kim and W. Choi, *J. Photochem. Photobiol., C*, 2013, **15**, 1–20.
2 A. Dąbrowski, P. Podkościelny, Z. Hubicki and M. Barczak, *Chemosphere*, 2005, **58**, 1049–1070.
3 K. Mondal, S. Bhattacharyya and A. Sharma, *Ind. Eng. Chem. Res.*, 2014, **53**, 18900–18909.
4 B. Liu and L. Peng, *J. Alloys Compd.*, 2013, **571**, 145–152.
5 J. Yu and X. Yu, *Environ. Sci. Technol.*, 2008, **42**, 4902–4907.
6 C. Wang, C. Shao, X. Zhang and Y. Liu, *Inorg. Chem.*, 2009, **48**, 7261–7268.
7 A. Weir, P. Westerhoff, L. Fabricius, K. Hristovski and N. von Goetz, *Environ. Sci. Technol.*, 2012, **46**, 2242–2250.
8 C. H. Kwon, H. Shin, J. H. Kim, W. S. Choi and K. H. Yoon, *Mater. Chem. Phys.*, 2004, **86**, 78–82.
9 K. Mondal, M. A. Ali, V. V. Agrawal, B. D. Malhotra and A. Sharma, *ACS Appl. Mater. Interfaces*, 2014, **6**, 2516–2527.
10 I. K. Konstantinou and T. A. Albanis, *Appl. Catal., B*, 2003, **42**, 319–335.
11 L. B. Reutergådh and M. Iangphasuk, *Chemosphere*, 1997, **35**, 585–596.
12 V. Augugliaro, L. Palmisano, M. Schiavello, A. Sclafani, L. Marchese, G. Martra and F. Miano, *Appl. Catal.*, 1991, **69**, 323–340.
13 Q. Zheng, H. J. Lee, J. Lee, W. Choi, N. B. Park and C. Lee, *Chem. Eng. J.*, 2014, **249**, 285–292.
14 W. Li, X. Cui, P. Wang, Y. Shao, D. Li and F. Teng, *Mater. Res. Bull.*, 2013, **48**, 3025–3031.
15 C. R. Chenthamarakshan, K. Rajeshwar and E. J. Wolfrum, *Langmuir*, 2000, **16**, 2715–2721.
16 M. R. Hoffmann, S. T. Martin, W. Choi and D. W. Bahnemann, *Chem. Rev.*, 1995, **95**, 69–96.
17 A. L. Linsebigler, G. Lu and J. T. Yates, *Chem. Rev.*, 1995, **95**, 735–758.
18 T. Nikawa, S.-i. Naya and H. Tada, *J. Colloid Interface Sci.*, 2015, **456**, 161–165.
19 N. Zhang, S. Liu, X. Fu and Y. J. Xu, *J. Phys. Chem. C*, 2011, **115**, 9136–9145.
20 Q. Xiang, J. Yu, B. Cheng and H. C. Ong, *Chem.–Asian J.*, 2010, **5**, 1466–1474.
21 V. R. De Mendonça, O. F. Lopes, R. P. Fregonesi, T. R. Giraldi and C. Ribeiro, *Appl. Surf. Sci.*, 2014, **298**, 182–191.
22 R. Asahi, T. Morikawa, T. Ohwaki, K. Aoki and Y. Taga, *Science*, 2001, **293**, 269–271.
23 F. Peng, L. Cai, H. Yu, H. Wang and J. Yang, *J. Solid State Chem.*, 2008, **181**, 130–136.
24 R. Liu, Y. Ren, Y. Shi, F. Zhang, L. Zhang, B. Tu and D. Zhao, *Chem. Mater.*, 2008, **20**, 1140–1145.
25 S. T. Hussain, K. Khan and R. Hussain, *J. Nat. Gas Chem.*, 2009, **18**, 383–391.
26 D. G. Huang, S. J. Liao, J. M. Liu, Z. Dang and L. Petrik, *J. Photochem. Photobiol., A*, 2006, **184**, 282–288.
27 D. Chen, D. Yang, Q. Wang and Z. Jiang, *Ind. Eng. Chem. Res.*, 2006, **45**, 4110–4116.
28 X. Wang, Y. Wang, L. Yang, K. Wang, X. Lou and B. Cai, *J. Power Sources*, 2014, **262**, 72–78.
29 S. Zhan, D. Chen, X. Jiao and C. Tao, *J. Phys. Chem. B*, 2006, **110**, 11199–11204.
30 Y.-Y. Song, Y.-H. Li, J. Guo, Z.-D. Gao and Y. Li, *J. Mater. Chem. A*, 2015, **3**, 23754–23759.
31 H. Jang, S.-K. Kim and S.-J. Kim, *J. Nanopart. Res.*, 2001, **3**, 141–147.
32 J. Du, J. Zhang and D. J. Kang, *CrystEngComm*, 2011, **13**, 4270–4275.
33 X. H. Yang, Z. Li, G. Liu, J. Xing, C. Sun, H. G. Yang and C. Li, *CrystEngComm*, 2011, **13**, 1378–1383.
34 T. Leshuk, S. Linley, G. Baxter and F. Gu, *ACS Appl. Mater. Interfaces*, 2012, **4**, 6062–6070.
35 H. Zhou, Y. Qu, T. Zeid and X. Duan, *Energy Environ. Sci.*, 2012, **5**, 6732–6743.
36 P. Hoyer and R. Könenkamp, *Appl. Phys. Lett.*, 1995, **66**, 349–351.
37 P. Wang, D. Li, J. Chen, X. Zhang, J. Xian, X. Yang, X. Zheng, X. Li and Y. Shao, *Appl. Catal., B*, 2014, **160–161**, 217–226.
38 X. Liu, L. Pan, T. Lv and Z. Sun, *J. Alloys Compd.*, 2014, **583**, 390–395.
39 X.-F. Gao, H.-B. Li, W.-T. Sun, Q. Chen, F.-Q. Tang and L.-M. Peng, *J. Phys. Chem. C*, 2009, **113**, 7531–7535.
40 K. P. Acharya, N. N. Hewa-Kasakarage, T. R. Alabi, I. Nemitz, E. Khon, B. Ullrich, P. Anzenbacher and M. Zamkov, *J. Phys. Chem. C*, 2010, **114**, 12496–12504.
41 K. P. Acharya, T. R. Alabi, N. Schmall, N. N. Hewa-Kasakarage, M. Kirsanova, A. Nemchinov, E. Khon and M. Zamkov, *J. Phys. Chem. C*, 2009, **113**, 19531–19535.
42 K. Tanaka, Y. Jin-nouchi, M. Fujishima and H. Tada, *J. Colloid Interface Sci.*, 2015, **457**, 248–253.
43 B.-R. Hyun, Y.-W. Zhong, A. C. Bartnik, L. Sun, H. D. Abruña, F. W. Wise, J. D. Goodreau, J. R. Matthews, T. M. Leslie and N. F. Borrelli, *ACS Nano*, 2008, **2**, 2206–2212.
44 K.-H. Lin, C.-Y. Chuang, Y.-Y. Lee, F.-C. Li, Y.-M. Chang, I. P. Liu, S.-C. Chou and Y.-L. Lee, *J. Phys. Chem. C*, 2011, **116**, 1550–1555.
45 J. Luo, L. Ma, T. He, C. F. Ng, S. Wang, H. Sun and H. J. Fan, *J. Phys. Chem. C*, 2012, **116**, 11956–11963.
46 R. Pan, Y. Wu and K. Liew, *Appl. Surf. Sci.*, 2010, **256**, 6564–6568.
47 K. Wang, S. Wan, Q. Liu, N. Yang and J. Zhai, *RSC Adv.*, 2013, **3**, 23755–23761.

Open Access Article. Published on 26 April 2016. Downloaded on 7/28/2025 12:12:42 PM.
This article is licensed under a Creative Commons Attribution-NonCommercial 3.0 Unported Licence.

Open Access Article. Published on 26 April 2016. Downloaded on 7/28/2025 12:12:42 PM.
This article is licensed under a Creative Commons Attribution-NonCommercial 3.0 Unported Licence.

48 G. Li, L. Wu, F. Li, P. Xu, D. Zhang and H. Li, *Nanoscale*, 2013, **5**, 2118–2125.
49 C. Su, C. Shao and Y. Liu, *J. Colloid Interface Sci.*, 2011, **359**, 220–227.
50 X. Li, T. Xia, C. Xu, J. Murowchick and X. Chen, *Catal. Today*, 2014, **225**, 64–73.
51 A. G. Kontos, V. Likodimos, E. Vassalou, I. Kapogianni, Y. S. Raptis, C. Raptis and P. Falaras, *Nanoscale Res. Lett.*, 2011, **6**, 1–6.
52 K. S. W. Sing, D. H. Everett, R. A. W. Haul, L. Moscou, R. A. Pierotti, J. RouqueroL and T. Siemieniewska, *Pure Appl. Chem.*, 1985, **57**, 603–619.
53 K. Mondal, J. Kumar and A. Sharma, *Colloids Surf., A*, 2013, **427**, 83–94.
54 T. Zhao, Z. Liu, K. Nakata, S. Nishimoto, T. Murakami, Y. Zhao, L. Jiang and A. Fujishima, *J. Mater. Chem.*, 2010, **20**, 5095–5099.
55 B. Fang, Y. Xing, A. Bonakdarpour, S. Zhang and D. P. Wilkinson, *ACS Sustainable Chem. Eng.*, 2015, **3**, 2381–2388.
56 N. Guijarro, T. Lana-Villarreal, I. Mora-Seró, J. Bisquert and R. Gómez, *J. Phys. Chem. C*, 2009, **113**, 4208–4214.
57 S.-C. Lin, Y.-L. Lee, C.-H. Chang, Y.-J. Shen and Y.-M. Yang, *Appl. Phys. Lett.*, 2007, **90**, 143517.
58 Q. Zhang, Y. Zhang, S. Huang, X. Huang, Y. Luo, Q. Meng and D. Li, *Electrochem. Commun.*, 2010, **12**, 327–330.
59 Y. Bessekhouad, N. Chaoui, M. Trzpit, N. Ghazzal, D. Robert and J. V. Weber, *J. Photochem. Photobiol., A*, 2006, **183**, 218–224.
60 O. Ahmed Zelekew and D.-H. Kuo, *Phys. Chem. Chem. Phys.*, 2016, **18**, 4405–4414.
61 A. Hernández-Gordillo, M. Arroyo, R. Zanella and V. Rodríguez-González, *J. Hazard. Mater.*, 2014, **268**, 84–91.
62 S. Gazi and R. Ananthakrishnan, *Appl. Catal., B*, 2011, **105**, 317–325.